H$_2$ and O$_2$ photocatalytic production on TiO$_2$ nanotube arrays: Effect of the anodization time on structural features and photoactivity

Marco Altomare [a], Michele Pozzi [a], Mattia Allieta [a], Luca Giacomo Bettini [b,c], Elena Selli [a,c,*]

[a] Dipartimento di Chimica, Università degli Studi di Milano, via Golgi 19, I-20133 Milano, Italy
[b] Dipartimento di Fisica, Università degli Studi di Milano, via Celoria 16, I-20133 Milano, Italy
[c] CIMaINa, Università degli Studi di Milano, via Celoria 16, I-20133 Milano, Italy

ABSTRACT

TiO$_2$ nanotube (NT) arrays of different lengths were prepared by electrochemical anodization of *ca.* 10 cm^2 area titanium disks in NH$_4$F–H$_2$O–formamide solution for different times, followed by annealing at 450 °C. After Pt deposition on the opposite side of the disk, the so obtained Ti-supported crystalline anodic oxides were employed as photoactive electrodes in a two compartments cell for separate H$_2$ and O$_2$ production through water photosplitting and characterized by SEM, XRD analysis and photocurrent measurements. The anodization time affected the phase composition and morphology of the growing NTs, which strictly influenced their photocatalytic activity. Short anodization times (40–60 min) resulted in well aligned short tubes composed of anatase-rutile mixed phases. Longer anodization (>2.5 h) yielded thicker NT arrays covered on top by a preferentially oriented anatase layer that limited their photoactivity. Photocurrent intensity measurements perfectly paralleled the water splitting activity results obtained with the different NT arrays. In particular, a square-shaped fast photoresponse was recorded with ordered and fully top-open nanotubular structures. On the other hand, clogged tubes not only yielded low current densities, but also showed delayed photocurrent transient signals due to the reduced mobility of the charge carriers within the preferentially oriented anatase layer. NT arrays obtained under optimized conditions had a *ca.* 80:20 anatase:rutile composition and ensured a hydrogen production rate of 83 mmol h^{-1} m^{-2} (*i.e.* 1.9 NL h^{-1} m^{-2}) in the absence of any hole scavenger or external bias.

© 2013 Elsevier B.V. All rights reserved.

1. Introduction

The production of hydrogen through the photocatalytic splitting of water [1] represents one of the main challenges in the current energy scenario. Up to date, TiO$_2$-based semiconductors are the most widely employed materials in photocatalysis [2], due to their relatively high efficiency, low cost, nontoxicity and photostability. However, conventional powder photocatalysts are not suitable for large-scale applications, not only because they exhibit fast charge recombination [3], limiting photoactivity, and need to be recovered from the aqueous media after their use, but mainly because they lead to the production of H$_2$ and O$_2$ mixtures, that must be subsequently separated and purified to attain the high-purity hydrogen required in most of the applications [4].

Thus, there is an urgent need to develop and optimize devices, which exploit supported thin layer photocatalysts, to generate separate H$_2$ and O$_2$ streams through water photosplitting [3–11]. One

dimensional TiO$_2$ nanostructures, such as nanotube (NT) arrays, meet these requirements, since they can be directly grown on a support material and also provide percolation pathways to photopromoted electrons [12,13], ensuring a more effective charge separation [14,15]. Furthermore, NT arrays, possessing high aspect ratio and surface area, guarantee enhanced photon absorption together with an extensive adsorption of reactant molecules on the photocatalyst surface [16], with beneficial effects on photoactivity.

Among the different preparation routes of semiconductor oxides, electrochemical anodization is the simplest and most versatile technique to synthesize these self-organized TiO$_2$ nanoarchitectures. In fact, the NTs properties and morphology can be tailored by controlling experimental parameters such as the anodization time, the applied DC voltage, the electrolyte composition and thermal treatment conditions [17].

In this work, a series of TiO$_2$ NT arrays grown by electrochemical anodization on a large surface (*ca.* 10 cm^2) titanium substrate has been tested as photoactive electrodes to separately produce H$_2$ and O$_2$ pure streams through photocatalytic water splitting in a two compartments cell [8], without any electrical bias or sacrificial agent. The photocatalytic behavior of these NT arrays is compared to their photocurrent response, which is very often

* Corresponding author at: Dipartimento di Chimica, Università degli Studi di Milano, via Golgi 19, I-20133, Italy. Tel.: +39 02 503 14237; fax: +39 02 503 14300.
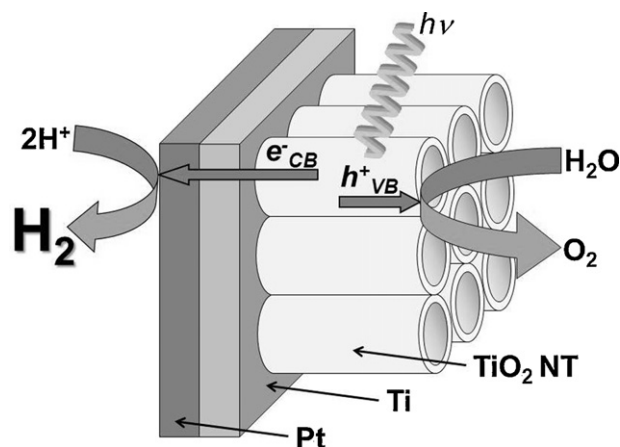*E-mail address:* elena.selli@unimi.it (E. Selli).

Fig. 1. Sketch of the TiO₂ NTs/Ti/Pt photoelectrode showing the mechanism of separate H₂ and O₂ production through photocatalytic water splitting.

employed as fast photocatalytic activity test. The photoactivity and photoelectrochemical results obtained with the different NT arrays are discussed in relation to the morphology and crystallographic features attained after different anodization times.

2. Experimental

2.1. Materials

Titanium disks (TI000420/15, ≥99.6%) were purchased from Goodfellow. Formamide (≥99.5%), NH_4F (≥98%), acetone (≥99%) and methanol (≥99.9%) were all Sigma–Aldrich chemicals. H_2SO_4 (95–97%) and NaOH (≥98.0%) were purchased from Fluka. Ultra-pure water (18.2 MΩ cm at 25 °C), supplied by a Millipore Direct-Q 3 water purification system, was used to prepare all solutions.

2.2. Preparation of the TiO₂ NT/Ti/Pt photoelectrodes

Self-assembled TiO₂ NT arrays were synthesized following a procedure reported in the literature [17]. After a thorough washing and degreasing by ultrasound treatment in acetone, methanol and water (10 min each), the titanium disks (0.5 mm thick, 40 mm in diameter) underwent anodization on one side, in a conventional two electrodes electrochemical cell connected to a DC power supply (Long Wei, PS-305D) under a 30 V applied potential. The side of the titanium disk in contact with the electrolyte solution and a platinum foil were the working and the counter electrode, respectively.

All experiments were carried out using a formamide-based electrolyte solution containing 0.6 wt.% NH_4F and 5 wt.% H_2O. The anodization time was varied from 20 min up to 7 h, to attain NTs layers characterized by different thickness. Then, the as-anodized oxides were soaked in ultrapure water, dried overnight in air at 70 °C and subsequently annealed in air at 450 °C for 3 h, with a heating ramp of 5 °C min⁻¹.

The preparation of the photoelectrodes for separate H₂ and O₂ production (see sketch in Fig. 1) was completed by Pt deposition on the non-anodized side of the titanium disks, after having grinded the surface with sandpaper (grit 1500, ca. 12.6 μm) to remove any surface oxide layer and establish a better Pt–Ti electric contact. A homogeneous thin Pt layer was obtained by room temperature DC sputtering [8], performed at 12 V and 20 mA for 14 min.

2.3. SEM and X-ray characterization

A scanning electron microscope (SEM, model LEO 1430, Zeiss) was employed to evaluate the effects induced by different anodization times on the TiO₂ NTs morphology.

X-ray diffraction (XRD) patterns were recorded with a Philips PW3020 diffractometer in the 20° < 2θ < 65° range (total counting time ca. 14 h), employing the Cu-K$_α$ radiation at room temperature. The diffraction data of all anodized layers were collected by placing the specimen directly within the sample compartment of the diffractometer.

The crystallographic phase composition of the anodized films was determined by Rietveld refinement performed using the GSAS software [18]. Structural models for anatase TiO₂, rutile TiO₂ and metallic Ti phases were taken from refs. [19] and [20]. The background was subtracted using the shifted Chebyshev polynomials and the diffraction peak profiles were fitted with a modified pseudo-Voigt function. The generalized spherical harmonic (GSH) model implemented in GSAS was used to account for the preferential orientation contribution to the diffracted intensities.

2.4. Photocatalytic activity

The TiO₂ NT/Ti/Pt photoelectrodes were tested in a two compartments photocatalytic Plexiglas cell, fully described elsewhere [8], allowing the separate evolution of pure hydrogen and oxygen from aqueous solutions. The two compartments of the cell were separated by the photoelectrode and were filled with 1.0 M NaOH and 0.5 M H_2SO_4 aqueous solutions, so that the anodic oxide was in contact with the alkaline solution, whereas the Pt-coated side faced the acidic solution. A small chemical bias was thus produced to assist electron transfer from the TiO₂ NT array toward the Pt-coated side of the photoelectrode (Fig. 1). Moreover, a cation exchange membrane (Nafion 117) was placed below the photoelectrode, in the frame separating the two cell compartments.

During irradiation, the evolved gases were collected within two upside-down graduated burettes surmounting each cell compartment [8]. The amounts of H₂ and O₂ were determined from the displacement of the solutions within each burette. The composition of the evolved gases was determined by gas chromatographic analysis, after having sampled them with a syringe. The irradiation source, always switched on 15 min prior to the beginning of the runs, was a UV–vis iron halogenide mercury arc lamp (Jelosil HG200, 250 W) with a full irradiation intensity of 3.12×10^{-8} Einstein s⁻¹ cm⁻² on the photocatalytic cell, as determined by ferrioxalate actinometry.

2.5. Photoelectrochemical characterization

Photocurrent measurements were performed in a two electrodes photoelectrochemical cell with a Pyrex glass window, through which the TiO₂ NT arrays were illuminated. The cell was filled with 1.0 M NaOH aqueous solution. The anodic oxides and a platinum foil were used as working and counter electrodes, respectively. The illumination was provided by a 150 W Xe lamp (Lot-Oriel Arc Lamp) coupled to a monochromator (Lot-Oriel Omni-λ 300). The lamp irradiance was measured with a Newport (818-UV) calibrated photodetector.

Incident photon to current conversion efficiency (IPCE) spectra were collected under monochromatic illumination in the absence of any applied electric bias, by measuring the photocurrent density with a digital multimeter (Agilent 34410A) in the 340–460 nm range. The multimeter and the monochromator were simultaneously operated by custom-built LabView software in order to acquire the steady short circuit photocurrent at each wavelength before moving to the next one.
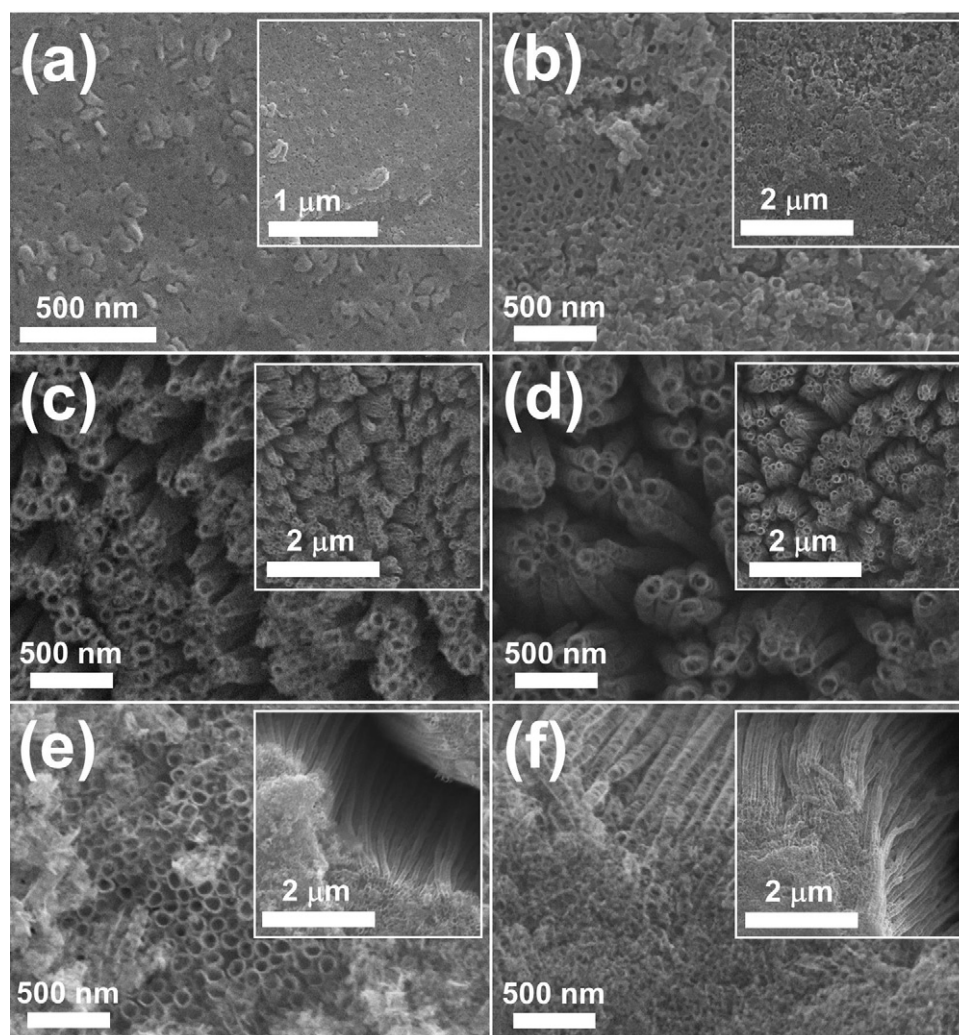
Fig. 2. SEM micrographs showing (a) the Ti disk surface prior to anodization and the NT arrays obtained after (b) 20 min, (c) 40 min, (d) 1 h, (e) 2.5 h and (f) 7 h anodization. Insets: top views of the samples at lower magnification.

Photocurrent transients were acquired by chronoamperometric measurements (current density *vs.* time) under chopped irradiation (60 s light/dark cycles) using a Gamry Ref600 potentiostat. All NTs samples were monochromatically irradiated at the wavelength for which their maximum IPCE was measured. The irradiation power was *ca.* 32 μW cm^{-2}.

3. Results and discussion

3.1. TiO$_2$ NTs morphology

Typical top-view micrographs of the samples are shown in Fig. 2(a)–(f), where the effect of different anodization times on the tubes morphology can be appreciated. When performing SEM analysis, the homogeneous morphology of all anodized surfaces was visually checked and always verified, before collecting representative images with different magnification. Generally, the thickness of the NTs layer increased with the anodization time, reaching values of several micrometers for long experiments [15]. The as-received Ti disk exhibited a flat surface (Fig. 2(a)), whereas the first pores within the TiO$_2$ surface appeared after 20 min anodization (sample NT1, Fig. 2(b)). This is in line with the NTs growth mechanism, resulting from both anodic oxide formation (titanium passivation) and its controlled chemical dissolution (TiO$_2$ etching) [15].

The 40 and 60 min-long anodization experiments (samples NT2 and NT3, see Fig. 2(c) and (d)) produced ordered nanotubular structures, homogeneously grown on the titanium substrate. In these samples, the NTs layer was a few micrometers thick. Longer anodization times (2.5 and 7 h, see Fig. 2(e) and (f)) led to the formation of NTs bundles separated by deep cracks. This cracked morphology, with NTs clumped together on the top, results from the mechanical stress occurring during the slow formation of the anodic oxide layer, typically observed for anodization in organic electrolytes [16,21].

Fig. 2(c) and (d) shows that top-open tubes were obtained after 40 and 60 min-long anodization experiments. This high aspect ratio morphology provided large surface area, suitable for efficient light absorption and high photocatalytic performance. On the contrary, NT arrays obtained after 2.5 and 7 h (Fig. 2(e) and (f)) exhibited an inhomogeneous top structure, partially or almost totally covered by a thin TiO$_2$ compact layer. During these experiments, a steady-state condition (*i.e.* constant current density) was on-going, leading to the thinning of the NTs walls, especially on the top side, where the NTs underwent etching in contact with the fluoride-containing electrolyte for long time [15]. Thus, the top structure collapsed as the NTs walls became too thin to withstand their own weight, leading to the formation of a compact oxide layer which clogged the tubes top [22].
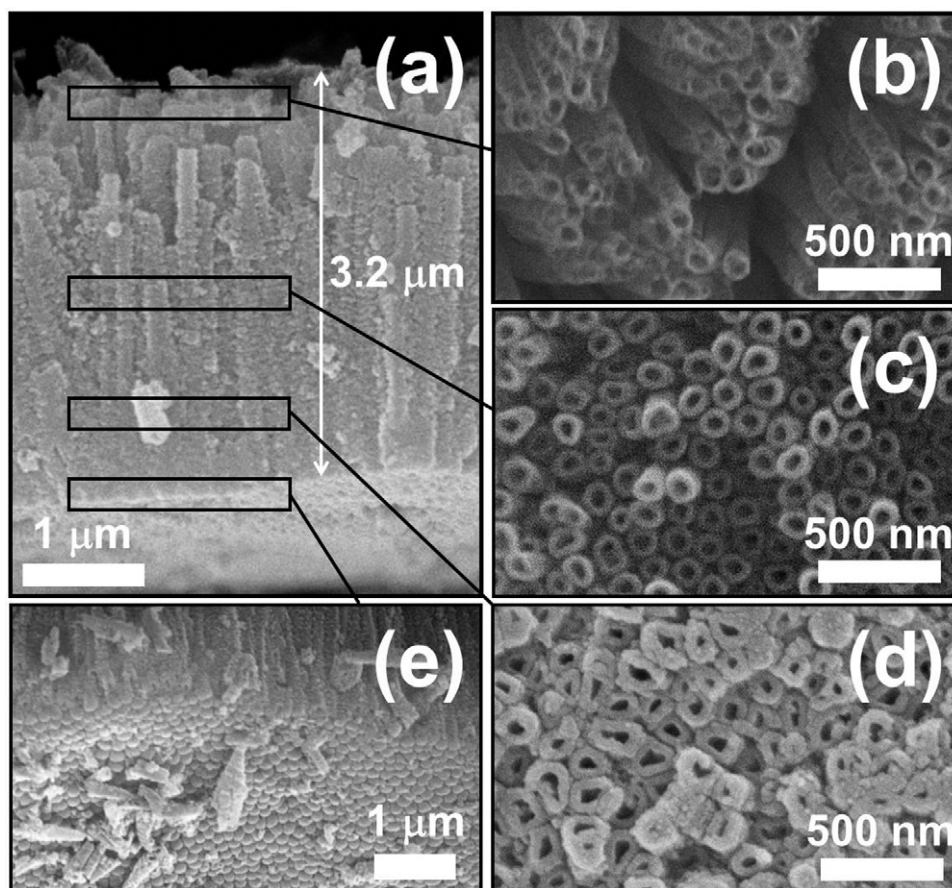
Fig. 3. SEM micrographs of the NT3 sample showing (a) the cross-section, the morphology (b) on the top, (c) at the middle and (d) near the bottom of the NT arrays and (e) their underneath structure.

However, in spite of these remarkable differences in morphology, the tubes diameter (when visible and not clogged) was always around 120–130 nm for all NT arrays, regardless of the anodization time (Fig. 2). This was expected since NTs diameter is mainly determined by the voltage applied during anodization [15,23].

Fig. 3(a) shows the cross-section micrograph of sample NT3, evidencing the typical columnar structure, with a thickness of *ca.* 3.2 μm. Fig. 3(b)–(d) show some SEM images taken at different heights along the NTs length. In particular, Fig. 3(b) shows that the tubes were clumped together on the top, while they were homogeneously packed and without cracks at middle height and close to their bottom, as shown in Fig. 3(c) and (d), respectively. Moreover, the NTs walls became thicker toward the bottom of the NTs layer. This wall thickness gradient is consistent with the typical morphology of TiO$_2$ NTs grown in organic electrolytes [15]. The underneath structure (*i.e.* the titanium–NTs interface) shown in Fig. 3(e) evidences that NTs were closed by a hemispherically-shaped bottom.

3.2. Crystallographic properties

The as-formed TiO$_2$ NT arrays are typically amorphous and can be converted into the anatase phase by annealing in air at temperatures above 280 °C. Anatase and rutile mixtures can be obtained at temperatures higher than 450 °C [24–28]. Our anodic oxides were annealed in air at 450 °C for 3 h.

In order to investigate the effect of the anodization time on the NTs composition after annealing, an XRD analysis was performed of the Ti disk and of the different NT arrays. The recorded XRD spectra are collected in Fig. 4(a). The diffraction peaks of the pristine Ti disk correspond to metallic Ti. With increasing the anodization

time, the intensity of the Ti signals decreased, while the diffraction peaks due to the anatase and rutile TiO$_2$ phases appeared, with the intensity of the anatase reflections increasing with the anodization time. This is consistent with the higher thickness of the TiO$_2$ NTs layers increasing with the anodization time. The phase composition of the anodic oxides was determined by Rietveld analysis, by refining the diffraction data against the anatase, rutile and titanium structural models. As an example, the Rietveld refinement for sample NT2 is shown in Fig. 4(b), while the refined lattice parameters and weight fractions of all NTs samples are reported in Table 1.

A plot of the refined weight fractions of the anatase and rutile phases as a function of the anodization time is shown in Fig. 5(a). After 20 min-long anodization, a 60:40 anatase:rutile mixture was obtained, while longer experiments led to an increase of the anatase content. In particular, the rutile phase almost disappeared (~3 wt.%) in sample NT4 obtained by 2.5 h-long anodization, whereas after 7 h (sample NT5) a nearly pure anatase NTs layer was obtained. This anodization time-dependent phase composition of the nanostructured anodic oxides can be ascribed to the initial nucleation of a thin rutile layer (50–100 nm) at the Ti–TiO$_2$ interface [22], followed by the formation of near pure anatase NTs. In other words, the rutile content was reasonably almost the same in all samples, whereas the amount of anatase phase increased with increasing the thickness of the NTs layer, so that the percent amount of rutile became negligible in samples anodized for long time.

The average TiO$_2$ crystallite sizes in the NT arrays, determined by applying the single peak method (*i.e.* the Scherrer equation) to the (1 0 1) and (1 1 0) reflections of the anatase and rutile phases, respectively, was found to be almost identical for both phases within each NTs sample, increasing from 25 to 34 nm for NT1–NT4,
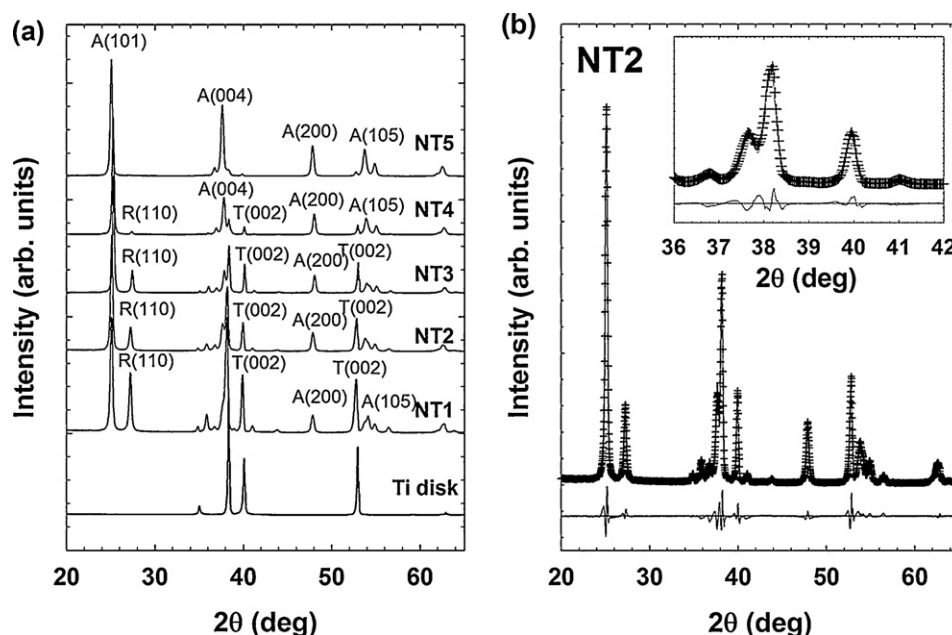
Fig. 4. (a) XRD patterns of the titanium disk and of the NT arrays, where the strongest reflections due to Ti (T) and to the anatase (A) and rutile (R) TiO$_2$ phases are marked in each pattern; (b) measured (crosses) and calculated (continuous lines) powder diffraction patterns of sample NT2. The difference between the observed and the fitted patterns is displayed at the bottom of this panel. The inset of panel (b) shows a magnified view of the middle angle diffraction peaks.
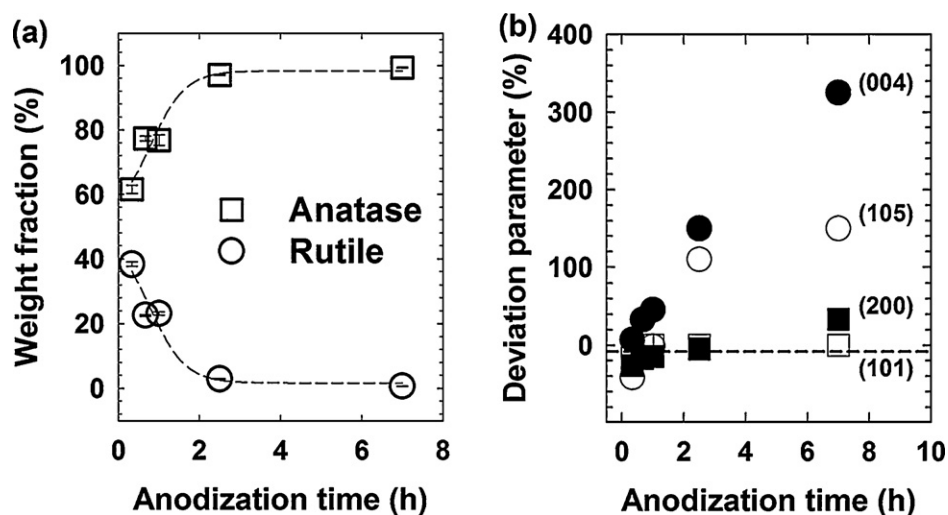

Fig. 5. (a) Refined weight percent fractions of the anatase and rutile phases in all TiO$_2$ NT arrays and (b) the corresponding deviation parameter $D(h\,k\,l)$ of the anatase (0 0 4), (1 0 5), (2 0 0) and (1 0 1) reflections, both plotted as a function of the anodization time. The dashed line in panel (b) marks the zero deviation for a random anatase powder.

while a slightly lower value (~29 nm) was obtained for the anatase phase in sample NT5.

The intensity of some anatase reflections increased with the anodization time more rapidly than others (Fig. 4(a)), a feature to be ascribed to preferential orientation effects, related to the anisotropic character of the TiO$_2$ microstructure. This effect was analyzed in terms of normalized intensities, determined by dividing the peaks intensity by the intensity of the maximum intensity (1 0 1) reflection. The preferential orientation effect was thus quantified in terms of the percent deviation parameter (D), calculated as

Table 1
Refined structural data of TiO$_2$ NT arrays produced by different anodization times, obtained from XRD analysis.

Anodization time	Sample	Anatase phase			Rutile phase		
		a (Å)	c (Å)	wt.%	a (Å)	c (Å)	wt.%
20 min	NT1	3.7819	9.482	61.6	4.5888	2.9580	38.4
40 min	NT2	3.7811	9.4910	77.3	4.5890	2.9589	22.7
60 min	NT3	3.7831	9.4967	76.8	4.5913	2.9597	23.2
2.5 h	NT4	3.7824	9.4998	97.1	4.5919	2.958	2.9
7 h	NT5	3.7804	9.4927	99.3	4.592	2.955	0.7

Table 2
Photocatalytic activity of the TiO_2 NT arrays in terms of H_2 and O_2 production rates (r_{H_2} and r_{O_2}), hydrogen productivity and apparent quantum efficiency Φ_{H_2}.

Sample	r_{H_2} [a] ($\mu mol\ h^{-1}$)	r_{O_2} [a] ($\mu mol\ h^{-1}$)	Productivity[b] ($NL_{H_2}\ m^{-2}h^{-1}$)	Φ_{H_2} [b] (%)
NT1	38 ± 5	23 ± 2	0.87	6.9
NT2	80 ± 8	43 ± 4	1.9	15
NT3	43 ± 7	23 ± 5	1.0	7.9
NT4	23 ± 3	12 ± 2	0.53	4.2
NT5	29 ± 6	14 ± 4	0.67	5.4

[a] Average values calculated over 3 photocatalytic runs.
[b] Values based on the data collected during the third photocatalytic run.

the percent difference between the normalized reflection intensities of the NTs oxide layers and the normalized reflection intensities of a fully random orientation, according to Eq. (1):

$$D(h\,k\,l)(\%) = \frac{I(h\,k\,l)_S - I(h\,k\,l)_P}{I(h\,k\,l)_p} \times 100 \qquad (1)$$

where $I(h\,k\,l)_S$ is the normalized intensity related to the $(h\,k\,l)$ peak of the NTs sample and $I(h\,k\,l)_P$ is the normalized intensity of the $(h\,k\,l)$ peak for the TiO_2 reference powder [19].

The $D(h\,k\,l)$ values relative to the main anatase reflections are plotted as a function of the anodization time in Fig. 5(b). The intensity of the $(2\,0\,0)$ reflection was in close agreement to that of isotropic anatase TiO_2, whereas the intensity of the $(1\,0\,5)$ and $(0\,0\,4)$ reflections showed positive deviation from the randomly oriented powder, increasing with increasing the anodization time. In particular, the $D(0\,0\,4)$ parameter for sample NT5 (7 h) reached a value 3 times higher ($D > 300\%$) than that of a random orientation.

It's worth underlining that the XRD diffraction data were collected in the reflection mode by placing the anodic layers parallel to the sample holder. Thus, the crystallographic planes parallel to the film surface mainly contributed to the diffracted intensities. According to SEM analysis and XRD data refinements, a compact and preferentially oriented anatase TiO_2 layer formed on the NTs top after long anodization times (>1 h), as well evidenced in Fig. 5(b) by the evolution of the $D(0\,0\,4)$ parameter with the irradiation time.

The formation of a preferentially oriented anodic oxide was very recently reported also by Lee et al. [29], who grew TiO_2 NTs with a specific crystallographic orientation by controlling the water content of the electrolyte during anodization. In our case, the preferential crystallographic orientation appears to be related to the compact anatase layer formed on top of the NTs after long anodization time (Fig. 2(e) and (f)), not to the NTs themselves.

3.3. H_2 production through photocatalytic water splitting

The photocatalytic activity of the TiO_2 NT arrays was evaluated by measuring the amount of H_2 and O_2 separately produced through water photosplitting in the photocatalytic cell [8], working without any electrical bias and in the absence of any hole scavenger. The results are collected in Table 2.

As sketched in Fig. 1, upon illumination of the TiO_2 NTs layer, electron–hole pairs are generated. Then, the photopromoted electrons migrate along the TiO_2 NTs and are transferred through the conductive titanium disk to the Pt film deposited on the opposite side of the photoelectrode, while the photoproduced holes remain confined in the TiO_2 valence band. Hence, photopromoted electrons e^- can reduce H^+ to H_2 in the cathodic side of the cell, while the holes h^+ can oxidize water to O_2 in the anodic compartment.

$$TiO_2 + h\nu \rightarrow e^- + h^+ \quad e^- - h^+ \quad \text{pair generation}$$

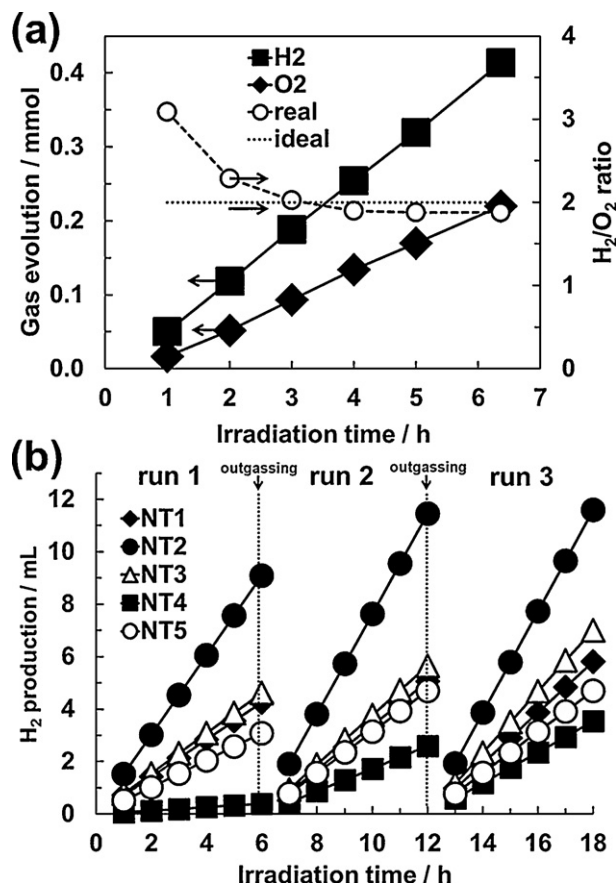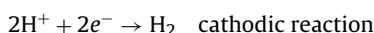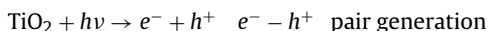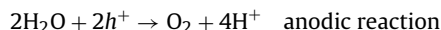$$2H^+ + 2e^- \rightarrow H_2 \quad \text{cathodic reaction}$$

Fig. 6. (a) H_2 and O_2 production under irradiation with sample NT2, together with the ideal (horizontal line) and measured (circles) H_2:O_2 ratio; (b) H_2 production during three consecutive 6 h–long runs with all NT arrays.

$$2H_2O + 2h^+ \rightarrow O_2 + 4H^+ \quad \text{anodic reaction}$$

The apparent quantum efficiency of H_2 production through photocatalytic water splitting (Φ_{H_2}, see Table 2) was calculated according to Eq. (2):

$$\Phi_{H_2}(\%) = \frac{2r_{H_2}}{IA} \times 100 \qquad (2)$$

where r_{H_2} is the rate of hydrogen production, I is the irradiation intensity on the TiO_2 NT arrays and A is the irradiated area (ca. 9.6 cm^2).

During irradiation, H_2 and O_2 evolved in the cathodic and anodic compartment of the photocatalytic cell, respectively, and accumulated in the upper part of the top burettes, which were outgassed through their upper stopcocks when required. Small traces of H_2 (always below 5 vol.%) were detected in the O_2 stream, probably due to the *in situ* reaction of photopromoted electrons with water also in the anodic side of the cell. On the other hand, pure H_2 was always found to evolve from the cathodic side of the cell.

In all photocatalytic tests, water photosplitting into hydrogen and oxygen occurred at almost constant rate and the H_2:O_2 ratio was always ca. 2, apart from an initial induction during the first 90 min of irradiation (see for example Fig. 6(a)). Moreover, with all NT arrays the amount of evolved H_2 noticeably increased during consecutive runs, as evidenced in Fig. 6(b), especially in the case of NT4. Considering all results, the photoactivity trend in water photosplitting was always NT2 ≫ NT3 > NT1 > NT5 ≈ NT4, even after 18 h – long photocatalysis. It's worth underlining that the r_{H_2} and r_{O_2} values reported in Table 2 are average values based on data collected

over three consecutive photocatalytic runs, and this explains their relatively high uncertainty.

Sample NT1 was characterized by a poor photocatalytic performance, probably because of its "immature" morphology, *i.e.* it was characterized just by scallop-shaped pores within the surface passivation layer and no nanotubular structure (Fig. 2(b)). This low photoactivity could also be partly ascribed to its high rutile content (Fig. 5(a)). In fact, in view of photocatalytic applications, the TiO_2 anatase phase is usually preferred because it allows higher electron mobility. Moreover, the anodic oxide layer in sample NT1 is expected not to be thick enough to grant full light absorption.

On the contrary, well organized and top-open NT arrays, such as those obtained in samples NT2 and NT3 (Fig. 2(c) and (d)), exhibited higher water photosplitting ability. Their mixed phase composition (*ca.* 80:20 anatase:rutile, very similar to that of benchmark TiO_2 P25 from Evonik), implied the formation of anatase-rutile heterojunctions, which granted improved charge transfer and photocatalytic properties, by enhancing the $e^- - h^+$ separation efficiency [22].

Although samples NT4 and especially NT5 were characterized by thicker TiO_2 NTs layers (Fig. 2(e) and (f)), their photocatalytic activity was clearly lower than that of thinner NT arrays, most probably because of the detrimental formation of the strongly (0 0 4)-preferentially oriented anatase phase which covered (partially or even totally) the top of the tubes. This compact layer clogged the tubes mouths, thus reducing their surface area and consequently their photocatalytic activity. Moreover, although thicker oxide layers may ensure full light absorption, this would result in extended $e^- - h^+$ recombination since the electrons, once photopromoted into the TiO_2 conduction band, have to migrate over a longer path through the NTs before reaching the Pt-coated side of the photoelectrodes. The compact layer on top of the tubes is also expected to decrease the conductive behavior of the samples. Indeed, the (0 0 4)-preferentially oriented anatase phase was shown to be characterized by reduced density and mobility of photogenerated charge carriers [30,31].

In conclusion, the photoactivity of NT arrays in photocatalytic water splitting reflects their morphology and phase composition, with NT2 showing the best performance in terms of H_2 production rate (*ca.* 83 mmol h^{-1} m^{-2} corresponding to 1.9 NL h^{-1} m^{-2}, see Table 2). These properties can be definitely attributed to the NT2 optimal tubes length, granting full light absorption as well as a restrained $e^- - h^+$ recombination, together with an ordered morphology of fully open NTs and an optimal mixed anatase-rutile composition [10,23].

3.4. Photocurrent measurements

Fig. 7(a) shows the IPCE spectra recorded with all TiO_2 NT arrays, obtained according to the following equation [32]:

$$IPCE(\%) = \frac{I_{SC}1240}{P_{light}\lambda} \times 100 \qquad (3)$$

where I_{sc} (A cm^{-2}) is the short circuit photocurrent density measured at a specific incident wavelength λ (nm) and P_{light} (W cm^{-2}) is the illumination power density at the same wavelength.

All NTs layers showed an absorption edge (IPCE > 1%) at *ca.* 400 nm, which is consistent with an energy band gap of about 3.1 eV, to be associated to the mixed anatase-rutile composition of the NTs [21]. No differences in the IPCE onset could be appreciated in relation to the different phase composition of the NT arrays. Moreover, the IPCE spectra profiles exhibited their maximum values, all above 10%, at different wavelengths, ranging from 350 nm for NT2 to 365 nm for NT4, reflecting different TiO_2 NTs morphologies and phase composition. The 40 min-long anodized NT2 array was best performing also in this type of photoactivity test, exhibiting the highest IPCE value of ~28%. The maximum IPCE trend
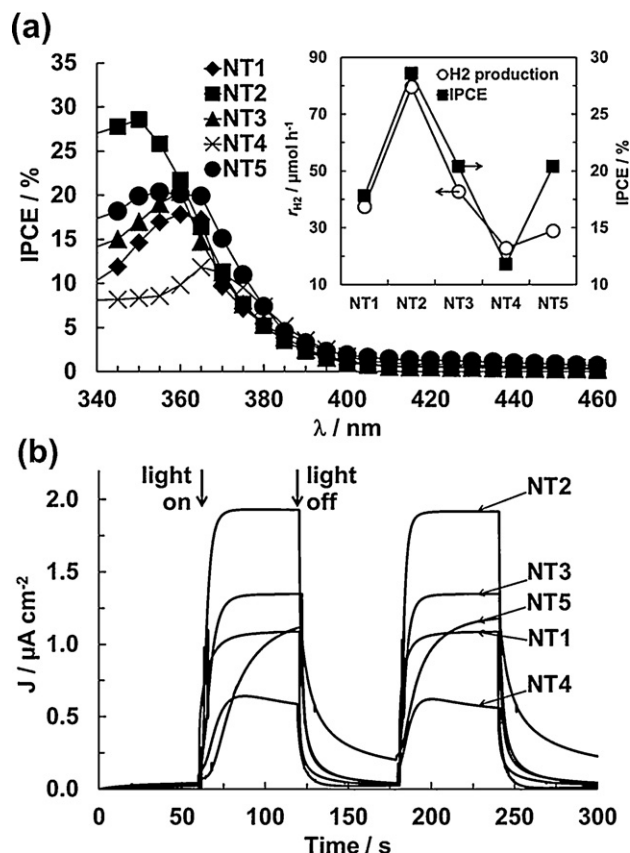

Fig. 7. (a) IPCE spectra, with the inset showing a comparison between the H_2 production rate r_{H_2} and the maximum IPCE value, and (b) photocurrent transient signals recorded under chopped (60 s on–off) monochromatic irradiation, for all TiO_2 NT arrays obtained by different anodization times.

followed the order NT2 > NT3 > NT5 > NT1 > NT4, with a significant variation of the IPCE maximum perfectly mirroring the photoactivity trend in H_2 production rate by water photosplitting, as outlined in the inset of Fig. 7(a). Thus the morphology and phase composition of NT arrays, obtained by anodization for different time followed by annealing, played a major role in determining both their photocatalytic and photo-electrochemical behavior. Furthermore, IPCE measurements confirm to be a fast way to get a photoactivity scale predicting that attainable in photocatalytic hydrogen production by water splitting.

Finally, the shape of the photocurrent transient signals, recorded with the different NTs layers in several 60 s-long light on–off cycles, provided further information on the photoresponse dynamics in relation to the structural features of the NT arrays. As shown in Fig. 7(b), fast photocurrent rise and decay during light–dark cycles, resulting in square-shaped reproducible current signals, were observed with samples NT1, NT2 and NT3, consisting of well aligned and fully top-open NTs. For these arrays, the dark current value was almost zero, while upon illumination the response quickly attained a steady-state value (1.0, 1.8 and 1.3 μA cm^{-2} for NT1, NT2 and NT3, respectively). This fast photoresponse indicates efficient charge separation and rapid electron migration toward the back contact [33].

On the contrary, a sort of capacitive behavior, consisting of an exponential raise and decay of the transient signals when the light was turned on and off, was recorded with NT4 and, in particular, with NT5 (Fig. 7(b)). Although these samples exhibited quite similar performance in photocatalytic water splitting (Table 2), sample NT4 showed a peculiar photoresponse curve (Fig. 7(a)) with the lowest IPCE maximum value, possibly due to the extended length

of the NTs and partial coverage of their top. On the other hand, NT5, resulting from a very long anodization time compared to the other NT arrays, essentially consisted of almost pure preferentially oriented compact anatase phase, able to fully absorb light and produce $e^- - h^+$ couples. This resulted in a relatively high IPCE signal (Fig. 7(b)). However, on the basis of time-resolved photoluminescence measurements [30], conduction band electrons generated within the (0 0 4) preferentially oriented anatase phase were recently shown to have low lifetime and mobility. Thus, in the NT5 sample, anodized for excessively long time, photopromoted electrons were retarded in their migration along the TiO_2 layer because of extended trap-filling predominantly occurring within the anatase layer grown on the NTs top.

4. Conclusions

Electrochemical anodization followed by annealing is shown to be an effective and easily tunable route to produce nanotubes layers supported on large surface photoelectrodes to be employed as active materials for the water splitting. The photocatalytic activity of these TiO_2 NT arrays is perfectly paralleled by their performance in photocurrent measurements, indicating that both their photocatalytic and photoelectrochemical behavior largely depend on the NTs length and top morphology. Moreover, this also confirms the reliability of relatively fast photocurrent measurements in predicting a photoactivity scale in H_2 production by water photosplitting. The anodization time length represents the key factor to produce well aligned and top-open NT arrays with an optimal aspect ratio, to be employed as photoactive materials in large area photoelectrodes for sustainable photocatalytic production of pure hydrogen.

Acknowledgements

References

[1] A. Fujishima, K. Honda, Nature 238 (1972) 637.
[2] X. Chen, S.S. Mao, Chemical Reviews 107 (2007) 2891.
[3] K. Fujihara, T. Ohno, M. Matsumura, Journal of the Chemical Society, Faraday Transactions 94 (1998) 3705.
[4] M. Kitano, M. Takeuchi, M. Matsuoka, J.M. Thomas, M. Anpo, Catalysis Today 120 (2007) 133.
[5] M. Kitano, R. Mitsui, D.R. Eddy, Z.M.A. El-Bahy, M. Matsuoka, M. Ueshima, M. Anpo, Catalysis Letters 119 (2007) 217.
[6] M. Kitano, M. Matsuoka, M. Ueshima, M. Anpo, Applied Catalysis A: General 325 (2007) 1.
[7] M. Matsuoka, M. Kitano, M. Takeuchi, K. Tsujimaru, M. Anpo, J.M. Thomas, Catalysis Today 122 (2007) 51.
[8] E. Selli, G.L. Chiarello, E. Quartarone, P. Mustarelli, I. Rossetti, L. Forni, Chemical Communications (2007) 5022.
[9] Y. Sun, G. Wang, K. Yan, International Journal of Hydrogen Energy 36 (2011) 15502.
[10] Y. Sun, K. Yan, G. Wang, W. Guo, T. Ma, Journal of Physical Chemistry C 115 (2011) 12844.
[11] R. Marschall, C. Klaysom, A. Mukherji, M. Wark, G.Q.M. Lu, L. Wang, International Journal of Hydrogen Energy 37 (2012) 4012.
[12] M. Law, J. Goldberger, P. Yang, Annual Review of Materials Research 34 (2004) 83.
[13] M. Grätzel, Inorganic Chemistry 44 (2005) 6841.
[14] R. Jennings, A. Ghicov, L.M. Peter, P. Schmuki, A.B. Walker, Journal of the American Chemical Society 130 (2008) 13364.
[15] P. Roy, S. Berger, P. Schmuki, Angewandte Chemie International Edition 50 (2011) 2904.
[16] G.K. Mor, O.K. Varghese, M. Paulose, K. Shankar, C.A. Grimes, Solar Energy Materials and Solar Cells 90 (2006) 2011.
[17] S. Rani, S.C. Roy, M. Paulose, O.K. Varghese, G.K. Mor, S. Kim, S. Yoriya, T.J. LaTempa, C.A. Grimes, Physical Chemistry Chemical Physics 12 (2010) 2780.
[18] R.B. Larson, ACVD, General Structural Analysis System, Los Alamos National Laboratory, 2004, 86.
[19] J.K. Burdett, T. Hughbanks, G.J. Miller, J.W. Richardson Jr., J.V. Smith, Journal of the American Chemical Society 109 (1987) 3639.
[20] R.R. Pawar, V.T. Deshpande, Acta Crystallographica A24 (1968) 316.
[21] Y. Liu, R.S. Alwitt, K. Shimizu, Journal of the Electrochemical Society 147 (2000) 1382.
[22] I. Paramasivam, H. Jha, N. Liu, P. Schmuki, Small 8 (2012) 3073.
[23] J.M. Macak, H. Tsuchiya, A. Ghicov, K. Yasuda, R. Hahn, S. Bauer, P. Schmuki, Current Opinion in Solid State & Materials Science 11 (2007) 3.
[24] J. Yu, B. Wang, Applied Catalysis B: Environmental 94 (2010) 295.
[25] O.K. Varghese, D. Gong, M. Paulose, C.A. Grimes, E.C. Dickey, Journal of Materials Research 18 (2003) 156.
[26] A. Ghicov, H. Tsuchiya, J.M. Macak, P. Schmuki, Physica Status Solidi A 203 (2006) R28.
[27] J.M. Macak, S. Aldabergerova, A. Ghicov, P. Schmuki, Physica Status Solidi A 203 (2006) R67.
[28] J. Zhao, X. Wang, T. Sun, L. Li, Nanotechnology 16 (2005) 2450.
[29] S. Lee, I.J. Park, D.H. Kim, W.M. Seong, D.W. Kim, G.S. Han, J.Y. Kim, H.S. Jung, K.S. Hong, Energy & Environmental Science 5 (2012) 7989.
[30] H.T. Tung, J.M. Song, S.W. Feng, C. Kuo, I.G. Chen, Physical Chemistry Chemical Physics 12 (2010) 740.
[31] Y. Xu, M.R. Shen, Applied Physics A 94 (2009) 275.
[32] O. Enea, J. Moser, M. Grätzel, Journal of Electroanalytical Chemistry 259 (1989) 59.
[33] A. Mazzarolo, K. Lee, A. Vicenzo, P. Schmuki, Electrochemistry Communications 22 (2012) 162.